

Current-induced motion of twisted skyrmions

Chendong Jin¹, Chunlei Zhang¹, Chengkun Song¹, Jinshuai Wang¹, Haiyan Xia¹, Yunxu Ma¹, Jianing Wang¹, Yurui Wei¹, Jianbo Wang^{1,2} and Qingfang Liu^{1,*}

¹Key Laboratory for Magnetism and Magnetic Materials of the Ministry of Education, Lanzhou University, Lanzhou 730000, People's Republic of China.

²Key Laboratory for Special Function Materials and Structural Design of the Ministry of the Education, Lanzhou University, Lanzhou 730000, People's Republic of China.

Abstract

Twisted skyrmions, whose helicity angles are different from that of Bloch skyrmions and Néel skyrmions, have already been demonstrated in experiments recently. In this work, we first contrast the magnetic structure and origin of the twisted skyrmion with other three types of skyrmion including Bloch skyrmion, Néel skyrmion and antiskyrmion. Following, we investigate the dynamics of twisted skyrmions driven by the spin transfer torque (STT) and the spin Hall effect (SHE) by using micromagnetic simulations. It is found that the spin Hall angle of the twisted skyrmion is related to the dissipative force tensor and the Gilbert damping both for the motions induced by the STT and the SHE, especially for the SHE induced motion, the skyrmion Hall angle depends substantially on the skyrmion helicity. At last, we demonstrate that the trajectory of the twisted skyrmion can be controlled in a two dimensional plane with a Gilbert damping gradient. Our results provide the understanding of current-induced motion of twisted skyrmions, which may contribute to the applications of skyrmion-based racetrack memories.

Keywords: Twisted skyrmion, spin transfer torque, spin Hall effect

*Corresponding author: Qingfang Liu, liuqf@lzu.edu.cn

Introduction

It has been recognized that the spin-polarized current-induced the motion and reversal of magnetic structures arises as a result of the spin transfer torque (STT) effect[1-4], which has attracted large interests due to the fundamental physics and potential applications in spintronic devices, such as magnetic random access memories (MRAMs)[5, 6], racetrack memories[7, 8], nano-oscillators[9-11] and logic devices[12-14]. Recently, it has been reported that the spin Hall effect (SHE)[15, 16], generated by the pure spin currents flowed from the heavy metal substrate due to the strong spin-orbit coupling at the interface of ferromagnet/heavy-metal, is an alternative efficient method to manipulate the magnetization dynamics in magnetic materials[17-20]. Compared with the STT, the SHE does not require currents flow through the magnetic layer, and then reducing the Joule heat and electromigration, i.e., avoiding the restricted effect of large current density in traditional STT devices[21].

Magnetic skyrmions are chiral spin magnetization structures with topological properties and can be divided into the following types according to different types of Dzyaloshinskii-Moriya interaction (DMI)[22-26]: (i) Bloch skyrmions are first discovered in bulk non-centrosymmetric B20-type lattice structures such as MnSi[27], FeCoSi[28-30], and FeGe[31, 32] due to the presence of bulk DMI; (ii) Néel skyrmions are observed in multilayered ultrathin films lacking inversion symmetry with strong spin-orbit coupling like Ir(111)/Fe[33], Ta/CoFeB[34] and Pt/Co[35] due to the presence of interfacial DMI; (iii) Antiskyrmions are reported in Heusler compounds such as MnPtSn[36] due to the presence of anisotropic DMI[37, 38]. Recently, at the interface of chiral bulk Cu_2OSeO_3 below a certain thickness, the so-called twisted skyrmions are demonstrated directly by the circularly polarized resonant elastic x-ray scattering, due to the breaking of translational symmetry at the surface of bulk ferromagnet[39, 40]. Up to now, the dynamics of twisted skyrmions driven by current have not been reported. Therefore, in this paper, on the basis of comparing the magnetic structure, origin and topological properties of the above four types of skyrmion, we focus on the dynamics of twisted skyrmions driven by the STT and the SHE and also analysis the simulation results by using Thiele's equations[41].

Micromagnetic simulation details

Our magnetic simulation results are performed by using the Object Oriented MicroMagnetic Framework (OOMMF) public code[42], which includes the additional modules for bulk DMI, interfacial DMI, anisotropic DMI and twisted DMI. The magnetization dynamics is described by numerically solving the Landau-Lifshitz-Gilbert (LLG) equation containing terms of the STT and the SHE[17, 20], as follow:

$$\frac{d\vec{m}}{dt} = -\gamma\vec{m} \times \vec{H}_{\text{eff}} + \alpha\vec{m} \times \frac{d\vec{m}}{dt} + \vec{\tau}_{\text{STT}} + \vec{\tau}_{\text{SHE}}, \quad (1)$$

where \vec{m} is the unit vector of the local magnetization, γ is the gyromagnetic ratio, α is the Gilbert damping, \vec{H}_{eff} is the effective field including the exchange field, anisotropy field, demagnetization field and DMI effective field. The STT term is expressed as

$$\vec{\tau}_{\text{STT}} = v_s \vec{m} \times \left(\frac{\partial \vec{m}}{\partial x} \times \vec{m} \right) + \beta v_s \left(\vec{m} \times \frac{\partial \vec{m}}{\partial x} \right), \quad (2)$$

where β is the non-adiabatic factor, and v_s is the velocity of the conduction electrons with the form $v_s = \frac{\gamma \hbar P}{2\mu_0 e M_s} J$, where J is the current density, e is the electron charge, P is the spin polarization, \hbar is the reduced Planck constant, μ_0 is the permeability of free space, and M_s is the saturation magnetization. The electrons flowing toward $+x$ direction when $v_s > 0$.

The SHE term is given by

$$\vec{\tau}_{\text{SHE}} = -\frac{\gamma \hbar}{2\mu_0 e M_s L} \theta_{\text{SH}} \vec{m} \times \vec{m} \times (\vec{z} \times \vec{j}_{\text{HM}}), \quad (3)$$

where L is the thickness of the magnetic layer with the value of 1 nm, θ_{SH} is the spin-Hall angle of Pt substrate with the value of 0.07, \vec{z} is the unit vectors of the surface normal direction, and \vec{j}_{HM} is the current density injected into the heavy metal.

In order to eliminate the influence of the boundary effect on the size and dynamics of skyrmions, the 2D plane is assumed to $500 \times 500 \times 1 \text{ nm}^3$ (length \times width \times thickness) with the mesh size of $1 \times 1 \times 1 \text{ nm}^3$, and the initial position of the skyrmion is set in the center of the 2D plane. The material parameters are chosen similar to Ref. [8]: saturation magnetization $M_s = 580 \times 10^3 \text{ A/m}$, exchange constant $A = 1.5 \times 10^{-11} \text{ J/m}$, perpendicular magnetic anisotropy constant

$K_u = 8 \times 10^5 \text{ J/m}^3$, and DMI strength $D_{\text{DMI}} = 2.5 \sim 3.5 \times 10^{-3} \text{ J/m}^2$.

Four types of skyrmions

According to the different helicity of skyrmions, there are four types of skyrmions: Bloch skyrmion, Néel skyrmion, antiskyrmion and twisted skyrmion as shown in Figs. 1(a)–(d), respectively. Figures 1(e)–(h) display the corresponding spatial profiles of the local magnetization across the skyrmions. It can be seen that the m_z of the four types of skyrmions are consistent, while the m_x and m_y of the four types of skyrmions are different, which again proves the different distribution of the in-plane magnetic moments of the four types of skyrmions. We emphasize that the distribution of the in-plane magnetic moments in the skyrmion structure is determined by the direction of the DMI vector, that is to say, the existence of the twisted skyrmion in this work is achieved by changing the DMI vector, which is much different as the reason that observed in the experiments. Figures 1(i)–(l) show the four types of DMIs: bulk DMI, interfacial DMI, anisotropic DMI and twisted DMI that promise the existence of the Bloch skyrmion, Néel skyrmion, antiskyrmion and twisted skyrmion, respectively. The four types of DMI considered in C4 symmetry can be written as:

$$\begin{aligned}
E_{\text{BulkDMI}} &= \frac{D}{2} \sum_i \vec{S}_i \times (\vec{S}_{i+\hat{x}} \times \hat{x} - \vec{S}_{i-\hat{x}} \times \hat{x} + \vec{S}_{i+\hat{y}} \times \hat{y} - \vec{S}_{i-\hat{y}} \times \hat{y}), \\
E_{\text{InterDMI}} &= \frac{D}{2} \sum_i \vec{S}_i \times (-\vec{S}_{i+\hat{x}} \times \hat{y} + \vec{S}_{i-\hat{x}} \times \hat{y} + \vec{S}_{i+\hat{y}} \times \hat{x} - \vec{S}_{i-\hat{y}} \times \hat{x}), \\
E_{\text{AnisoDMI}} &= \frac{D}{2} \sum_i \vec{S}_i \times (\vec{S}_{i+\hat{x}} \times \hat{y} - \vec{S}_{i-\hat{x}} \times \hat{y} + \vec{S}_{i+\hat{y}} \times \hat{x} - \vec{S}_{i-\hat{y}} \times \hat{x}), \\
E_{\text{TwisDMI}} &= \frac{D}{2} \sum_i \vec{S}_i \times (\vec{S}_{i+\hat{x}} \times (\hat{x} - \hat{y}) + \vec{S}_{i-\hat{x}} \times (-\hat{x} + \hat{y}) + \vec{S}_{i+\hat{y}} \times (\hat{x} + \hat{y}) - \vec{S}_{i-\hat{y}} \times (\hat{x} + \hat{y})),
\end{aligned} \tag{4}$$

where D is the DMI constant representing the DMI strength, \vec{S}_i is the atomic moment unit vector, \hat{x} and \hat{y} are the unit vectors in the model.

Topological properties of four types of skyrmions

A. Helicity, winding number and topological number

In order to better understand the helicity and winding number of skyrmions, we use the two-dimensional polar coordinates to describe a general magnetic skyrmion structure, as shown in Fig. 2 which displays a Bloch skyrmion, as

example, in the polar coordinates with azimuthal angle (φ) and radial coordinate (ρ). Therefore, the unit vector of the local magnetization m_x , m_y and m_z in the Cartesian coordinates can be written as[26, 43, 44]:

$$\begin{aligned} m_x &= \sin \theta(\rho) \cos \phi(\varphi), \\ m_y &= \sin \theta(\rho) \sin \phi(\varphi), \\ m_z &= \cos \theta(\rho), \end{aligned} \tag{5}$$

where $\theta(\rho)$ is the radial profile of the perpendicular component of the magnetization, and from the center to the boundary, its value changes from -0.5π to 0.5π , $\phi(\varphi)$ is the angle between the magnetic moment and the radial coordinate. The vorticity of skyrmions is obtained by calculating the full turns of the transverse magnetic moments on the perimeter and is defined by the winding number[45] $W = \frac{1}{2\pi} \int_{\varphi=0}^{2\pi} d\phi(\varphi)$. Therefore, the winding number $W = 1$ for twisted skyrmion, Bloch skyrmion and Néel skyrmion as shown in Fig. 3(a), and $W = -1$ for antiskyrmion as shown in Fig. 3(b). The helicity of a skyrmion is given by $\chi = \phi(\varphi) - W \cdot \varphi = \phi(\varphi = 0)$ with the value ranging from $-\pi$ to π , that is, for the Bloch skyrmion, $\chi = \pm 0.5\pi$; for Néel skyrmion, $\chi = 0$ or π ; for twisted skyrmion, $\chi \neq \pm 0.5\pi, 0$ and π , and the helicity χ of the twisted skyrmion shown in Fig. 1 (d) equals to 0.25π ; for antiskyrmion as shown in Fig. 1(c), $\chi = \pi$. The topological number Q relates to the winding number and counts how many times the unit vector along the magnetic moment wraps the unit sphere with the form[26]

$$Q = \frac{1}{4\pi} \iint q dx dy, \quad q = \vec{m} \cdot \left(\frac{\partial \vec{m}}{\partial x} \times \frac{\partial \vec{m}}{\partial y} \right), \tag{6}$$

where q is the topological density. Figures 3(c) and (d) show the topological densities corresponding to the magnetic skyrmions shown in Figs. 3(a) and (b), respectively. It can be seen that $Q = -1$ in Fig. 3(c) and $Q = 1$ in Fig. 3(d), i.e., $Q = -W$ when the spins point down in the central region and point up in the boundary region.

B. Skyrmion size and dissipative force tensor

The diameter of twisted skyrmion size (d) is usually defined as the distance from in-plane to in-plane magnetization, i.e., the distance between the region $m_z = 0$, as shown in the inset of Fig. 4. The dissipative force tensor \mathcal{D} is used to describe the effect of the dissipative forces on the moving skyrmion[46-48]. For a single twisted skyrmion, \mathcal{D} is given by

$$\mathcal{D} = 4\pi \begin{pmatrix} \mathcal{D} & 0 \\ 0 & \mathcal{D} \end{pmatrix}, \quad \mathcal{D} = \frac{1}{4\pi} \int \frac{\partial \vec{m}}{\partial x} \cdot \frac{\partial \vec{m}}{\partial x} dx dy, \quad (7)$$

where \mathcal{D} is the diagonal element of the dissipative tensor and also called dissipative parameter. The dissipative parameter \mathcal{D} is determined by the diameter and domain wall width of the twisted skyrmion. Therefore, both d and \mathcal{D} are affected by DMI strength as shown in Fig. 4. With the increase in D_{DMI} from 2.5 to 3.5 mJ/m², d increases from 7.9 to 34.8 nm and \mathcal{D} increases from 1.0577 to 1.961, respectively, for the twisted skyrmion.

Dynamics of twisted skyrmion driven by the STT

To understand the STT-induced motion of the twisted skyrmions, we first use the Thiele equation[41] to describe the dynamics of the four kinds of skyrmions mentioned above by casting the LLG Eqs. (1) and (2) to the following equation[46, 47]:

$$\mathbf{G} \times (\mathbf{v}_s - \mathbf{v}_d) + \mathcal{D}(\beta \mathbf{v}_s - \alpha \mathbf{v}_d) = 0, \quad (8)$$

where \mathbf{G} is the gyrovector with the form $\mathbf{G} = (0 \ 0 \ G) = (0 \ 0 \ 4\pi Q)$, and \mathbf{v}_d is the drift velocity of the skyrmion. When the velocity of the conduction electrons \mathbf{v}_s applied along the x direction, $\mathbf{v}_d = (v_x, v_y)$ is derived from Eq. (8) as

$$\begin{cases} v_x = \left(\frac{\beta}{\alpha} + \frac{Q^2(\alpha - \beta)}{\alpha(Q^2 + \alpha^2 \mathcal{D}^2)} \right) v_s, \\ v_y = Q \frac{\mathcal{D}(\alpha - \beta)}{Q^2 + \alpha^2 \mathcal{D}^2} v_s. \end{cases} \quad (9)$$

It can be seen that the direction of the skyrmion deviates from the direction of the conduction electrons when $\alpha \neq \beta$, and this phenomenon is called the skyrmion Hall effect and can be further defined by the skyrmion Hall angle

$$\theta_{\text{sky}} = \text{sign}(v_y) \cdot \arccos\left(\frac{v_x}{\sqrt{v_x^2 + v_y^2}}\right), \quad (10)$$

which defines the angle in the range from -180° to 180° . For the situation of STT-induced skyrmion motion, the sign of the v_x is always the same with v_s , i.e., the skyrmion Hall angle is in the range of $(-90^\circ, 90^\circ)$, and therefore the Eq. (10) can

be reduced to $\theta_{\text{sky}} = \arctan\left(\frac{Q\mathcal{D}(\alpha - \beta)}{Q^2 + \alpha\beta\mathcal{D}^2}\right)$.

The trajectories of the four types of skyrmion driven by the in-plane STT with $v_s = 100$ m/s, $\alpha = 0.4$, $\beta = 0.2$ and

$D_{\text{DMI}} = 3 \text{ mJ/m}^2$ is shown in Fig. 5. The positions of the skyrmions are obtained by solving the guiding center (R_x, R_y) with the form[49, 50]

$$R_x = \frac{\iint xqdx dy}{\iint qdx dy}, \quad R_y = \frac{\iint yqdx dy}{\iint qdx dy}, \quad (11)$$

where q is the topological density. One can see that the antiskyrmion deflects to the $+y$ direction, while for Bloch skyrmion, Néel skyrmion and twisted skyrmion deflect to the $-y$ direction, i.e., θ_{sky} of the skyrmions with $Q = 1$ (antiskyrmion) and $Q = -1$ (Bloch, Néel and twisted skyrmion) equal to 12.89° and -12.89° , respectively. Following we focus on the STT-induced motion of twisted skyrmion with different conditions, as shown in Fig. 6. Figures 6 (a) and (b) show the v_x and v_y as a function of v_s for different α with $\beta = 0.2$ and $D_{\text{DMI}} = 3 \text{ mJ/m}^2$, respectively. It can be seen that v_x and v_y both increase linearly with the increase in v_s for different α , it should be also note that v_y is a negative value for $\alpha < \beta$, a positive value for $\alpha > \beta$, and zero for $\alpha = \beta$. Then we chose the situation of $v_s = 100 \text{ m/s}$ to investigate the skyrmion Hall angle of the twisted skyrmion as a function of v_s , as shown in Fig. 6(c), the skyrmion Hall angle θ_{sky} remains almost unchanged with the increase in v_s . Figure 6(d) shows the simulation and calculation of θ_{sky} as a function of α with $\beta = 0.2$, the skyrmion Hall angle θ_{sky} decreases from 13.7° to -12.89° with the α increasing from 0.01 to 0.4. According to Eqs. (9) and (10), both the velocity and the skyrmion Hall angle θ_{sky} are affected by the dissipative parameter \mathcal{D} , and the dissipative parameter \mathcal{D} is determined by the DMI strength D_{DMI} . Therefore, it is necessary to investigate the dynamics of the twisted skyrmion under different D_{DMI} , as shown in Figs. 6 (e) and (f) with $v_s = 100 \text{ m/s}$, $\alpha = 0.4$ and $\beta = 0.2$. v_x increases at first and then decreases with D_{DMI} increasing from 2.5 to 3.5 mJ/m^2 , while v_y keeps decreasing (the absolute value of v_y is continuously increasing), and both simulation and calculation results support that the corresponding skyrmion Hall angle θ_{sky} decreases from -11.4° to -16.8° (the absolute value of θ_{sky} is proportional to the D_{DMI}).

We have known that the STT-induced twisted skyrmion motion is affected by the damping in the previous paragraph. Following, we investigate the dynamics of twisted skyrmion induced by the STT under a damping gradient, as shown in Fig. 7. Figure 7(a) shows the position along the y axis of the twisted skyrmion as a function of distance along the x axis

with $v_s = 100$ m/s, $\beta = 0.4$ and $D_{\text{DMI}} = 3$ mJ/m². The damping decreases from 0.5 to 0.25 linearly from 0 to 50 nm along the x axis, as indicated by the color code. Figure 7 (b) shows the skyrmion Hall angle θ_{sky} of the twisted skyrmion as a function of its position along the x axis. In the region $\alpha > \beta$, the twisted skyrmion moves along the x axis direction from 0 nm and deflects in the $-y$ direction until moving to the x axis of 20 nm, where $\alpha = \beta = 0.4$; from the region of 20 to 50 nm along x axis, the twisted skyrmion begins to deflect in the $+y$ direction because of $\alpha < \beta$. Therefore, the trajectory of twisted skyrmion induced by the STT can be controlled under a damping gradient.

Dynamics of twisted skyrmion driven by the SHE

SHE-induced motion of antiskyrmion has already been studied in Ref. [38], which demonstrates that the antiskyrmion Hall angle depends on the direction of the current strongly. In this section, we focus on the SHE-induced motions of the skyrmions whose winding number $W = 1$ (Bloch, Néel and twisted skyrmion). The LLG Eqs. (1) and (3) can be cast into the following form:

$$\mathbf{G} \times \mathbf{v}_d + \alpha \mathcal{D} \mathbf{v}_d - 4\pi B \mathbf{R}(\chi) J_{\text{HM}} = 0 \quad (12)$$

where $\mathbf{G} = (0 \ 0 \ -4\pi)$ due to $Q = -1$, B is linked to the SHE, and the sign of B is determined by the SHE angle; $\mathbf{R}(\chi)$ is the in-plane rotation matrix with the form $\mathbf{R}(\chi) = \begin{pmatrix} \cos \chi & \sin \chi \\ -\sin \chi & \cos \chi \end{pmatrix}$ [49, 51]. When the current J_{HM} injected into the heavy metal along the x direction, $\mathbf{v}_d = (v_x, v_y)$ is derived from Eq. (12) as

$$\begin{cases} v_x = B \frac{\alpha \mathcal{D} \cos \chi + \sin \chi}{1 + \alpha^2 \mathcal{D}^2} J_{\text{HM}}, \\ v_y = B \frac{-\alpha \mathcal{D} \sin \chi + \cos \chi}{1 + \alpha^2 \mathcal{D}^2} J_{\text{HM}}. \end{cases} \quad (13)$$

The skyrmion Hall angle θ_{sky} can be obtained by the Eq. (10), which is in the range of -180° to 180° .

The Eq. (13) suggests that the direction of motion of the skyrmions depends on their helicities. Therefore, we first investigate the trajectories of skyrmions driven by the SHE with $J_{\text{HM}} = 10 \times 10^{10}$ A/m², $\alpha = 0.2$ and $D_{\text{DMI}} = 3$ mJ/m² for different helicities of skyrmions, as shown in Fig. 8. These skyrmions with different helicities are achieved by changing the direction of DMI vector. The simulation results in Fig. 8(a) show that the skyrmion Hall angles θ_{sky} are -150.4° ,

165.4°, 121.4°, 75.6°, 29.6°, -14.6°, -58.6° and -104.4° for the helicities $\chi = -0.75\pi, -0.5\pi, -0.25\pi, 0, 0.25\pi, 0.5\pi, 0.75\pi$ and π , respectively. Figure 8(b) shows the skyrmion Hall angle as a function of the helicity both supported by simulations and calculations. Following we take the case of $\chi = 0.25\pi$ (the twisted skyrmion shown in Fig. 1(d)) and investigate the motion induced by the SHE, as shown in Fig. 9. Figure 9(a) shows the simulation results of v_x and v_y of the twisted skyrmion as a function of J_{HM} with $\alpha = 0.2$ and $D_{\text{DMI}} = 3 \text{ mJ/m}^2$. It can be seen that v_x and v_y both increase linearly with the increase in J_{HM} , and the corresponding skyrmion Hall angle θ_{sky} is shown in Fig. 9(b). The skyrmion Hall angle θ_{sky} almost remains at 29.6° when J_{HM} is no more than $200 \times 10^{10} \text{ A/m}^2$, while for the case $J_{\text{HM}} = 500 \times 10^{10} \text{ A/m}^2$, the skyrmion Hall angle θ_{sky} decreases to 28.9°. This is because the size of the twisted skyrmion, i.e., the dissipative parameter \mathcal{D} , increases slightly with J_{HM} increasing to $500 \times 10^{10} \text{ A/m}^2$, the skyrmion Hall angle Eq. (10) can be reduced to

$$\theta_{\text{sky}} = \arctan\left(\frac{1 - \alpha\mathcal{D}}{1 + \alpha\mathcal{D}}\right). \quad (14)$$

For $\chi = 0.25\pi$, which indicates that the skyrmion Hall angle θ_{sky} decreases with the increase in \mathcal{D} . Figure 9(c) shows the simulation results of v_x and v_y of the twisted skyrmion as a function of α with $J_{\text{HM}} = 100 \times 10^{10} \text{ A/m}^2$ and $D_{\text{DMI}} = 3 \text{ mJ/m}^2$, v_x first increases and then decreases with α increasing from 0.01 to 1, while v_y keeps decreasing (the absolute value of v_y decreases at first and then increases), and therefore the corresponding skyrmion Hall angle θ_{sky} decreases from 44.3° to -8.2° (the trend of θ_{sky} is consistent with v_y), which also supported by calculation, as shown in Fig. 9(d). Figure 9(e) shows that v_x and v_y both increases with D_{DMI} increasing from 2.5 to 3.5 mJ/m^2 when $J_{\text{HM}} = 100 \times 10^{10} \text{ A/m}^2$ and $\alpha = 0.2$. Figure 9(f) shows that the corresponding skyrmion Hall angle θ_{sky} decreases with the increase in D_{DMI} , which is similar to the results by calculating the Eq. (14) with the increase in \mathcal{D} .

In contrast to the STT-induced twisted skyrmion motion under a damping gradient, we investigate the dynamics of twisted skyrmion driven by the SHE under a damping gradient, as shown in Fig. 10. Figure 10(a) shows the trajectory of the twisted skyrmion as a function of its position along the x axis with $J_{\text{HM}} = 100 \times 10^{10} \text{ A/m}^2$ and $D_{\text{DMI}} = 3 \text{ mJ/m}^2$. The damping increases from 0.2 to 1.2 linearly from 0 to 200 nm along the x axis, as indicated by the color code. Figure 10 (b)

shows the corresponding skyrmion Hall angle θ_{sky} as a function of its position along the x axis. The Eq. (14) implies that: in the region $1-\alpha\mathcal{D} > 0$, the twisted skyrmion moves along the x axis direction from 0 nm and deflects in the $+y$ direction until moving to the x axis of 114 nm where $1-\alpha\mathcal{D} = 0$; in the region $1-\alpha\mathcal{D} < 0$, i.e., from 114 to 200 nm along x axis, the twisted skyrmion deflects in the $-y$ direction. Therefore, the trajectory of the SHE-induced motion of twisted skyrmion can also be controlled by a damping gradient.

Conclusions

In summary, we first introduce the magnetic structure and the corresponding DMI of the twisted skyrmion in contrast to that of Bloch skyrmion, Néel skyrmion and antiskyrmion. Furthermore, we discuss and calculate the helicity, winding number, topological number, size and dissipative force tensor of the twisted skyrmion, which pave the way for the following study of the dynamics of twisted skyrmion driven by the STT and the SHE. For the STT-induced motion of twisted skyrmion, it is found that the skyrmion Hall angle is determined by the topological number, the dissipative force tensor and the difference between the Gilbert damping and the non-adiabatic factor. For the SHE-induced motion of twisted skyrmion, apart from the dissipative force tensor and the Gilbert damping, the skyrmion angle depends on the helicity significantly. At last, we demonstrate that the trajectories of both the STT-induced and the SHE-induced motion of twisted skyrmion can be controlled by a Gilbert damping gradient. These results may present guidance for the design of twisted skyrmion-based racetrack memories.

Acknowledgments

This work is supported by National Science Fund of China (11574121 and 51771086). C. J. acknowledges the funding by the China Scholarship Council.

References

- [1] J.C. Slonczewski, Current-driven excitation of magnetic multilayers, *J. Magn. Magn. Mater.* **159**, L1 (1996).
- [2] L. Berger, Emission of spin waves by a magnetic multilayer traversed by a current, *Phys. Rev. B* **54**, 9353 (1996).
- [3] S. Zhang, Z. Li, Roles of nonequilibrium conduction electrons on the magnetization dynamics of ferromagnets, *Phys. Rev. Lett.* **93**, 127204 (2004).
- [4] A. Brataas, A.D. Kent, H. Ohno, Current-induced torques in magnetic materials, *Nat. Mater.* **11**, 372 (2012).
- [5] Y. Huai, Spin-transfer torque MRAM (STT-MRAM): Challenges and prospects, *AAPPS bulletin* **18**, 33 (2008).

- [6] T. Kawahara, K. Ito, R. Takemura, H. Ohno, Spin-transfer torque RAM technology: Review and prospect, *Microelectron. Reliab.* **52**, 613 (2012).
- [7] S.S. Parkin, M. Hayashi, L. Thomas, Magnetic domain-wall racetrack memory, *Science* **320**, 190 (2008).
- [8] J. Sampaio, V. Cros, S. Rohart, A. Thiaville, A. Fert, Nucleation, stability and current-induced motion of isolated magnetic skyrmions in nanostructures, *Nat. Nanotechnol.* **8**, 839 (2013).
- [9] Z. Zeng, G. Finocchio, H. Jiang, Spin transfer nano-oscillators, *Nanoscale* **5**, 2219 (2013).
- [10] S. Zhang, J. Wang, Q. Zheng, Q. Zhu, X. Liu, S. Chen, C. Jin, Q. Liu, C. Jia, and D. Xue, Current-induced magnetic Skyrmions oscillator, *New J. Phys.* **17**, 023061 (2015).
- [11] C. Jin, J. Wang, W. Wang, C. Song, J. Wang, H. Xia, Q. Liu, Array of Synchronized Nano-Oscillators Based on Repulsion between Domain Wall and Skyrmion, *Phys. Rev. Applied* **9**, 044007 (2018).
- [12] D.A. Allwood, G. Xiong, C. Faulkner, D. Atkinson, D. Petit, R. Cowburn, Magnetic domain-wall logic, *Science* **309** 1688 (2005).
- [13] M. Hayashi, L. Thomas, R. Moriya, C. Rettner, S.S. Parkin, Current-controlled magnetic domain-wall nanowire shift register, *Science* **320**, 209 (2008).
- [14] X. Zhang, M. Ezawa, Y. Zhou, Magnetic skyrmion logic gates: conversion, duplication and merging of skyrmions, *Sci. Rep.* **5**, 9400 (2015).
- [15] S. Emori, U. Bauer, S.-M. Ahn, E. Martinez, G.S. Beach, Current-driven dynamics of chiral ferromagnetic domain walls, *Nat. Mater.* **12**, 611 (2013).
- [16] L. Liu, C.-F. Pai, Y. Li, H. Tseng, D. Ralph, R. Buhrman, Spin-torque switching with the giant spin Hall effect of tantalum, *Science*, **336**, 555 (2012).
- [17] R. Tomasello, E. Martinez, R. Zivieri, L. Torres, M. Carpentieri, and G. Finocchio, A strategy for the design of Skyrmion racetrack memories, *Sci. Rep.* **4**, 6784 (2014).
- [18] C. Jin, C. Song, J. Wang, and Q. Liu, Dynamics of antiferromagnetic Skyrmion driven by the spin Hall effect, *Appl. Phys. Lett.* **109**, 182404 (2016).
- [19] H. Ulrichs, V. Demidov, S. Demokritov, Micromagnetic study of auto-oscillation modes in spin-Hall nano-oscillators, *Appl. Phys. Lett.* **104**, 042407 (2014).
- [20] E. Martinez, S. Emori, G.S. Beach, Current-driven domain wall motion along high perpendicular anisotropy multilayers: The role of the Rashba field, the spin Hall effect, and the Dzyaloshinskii-Moriya interaction, *Appl. Phys. Lett.* **103**, 072406 (2013).
- [21] V. Demidov, S. Urazhdin, E. Edwards, S. Demokritov, Wide-range control of ferromagnetic resonance by spin Hall effect, *Appl. Phys. Lett.* **99**, 172501 (2011).
- [22] I. Dzyaloshinsky, A thermodynamic theory of “weak” ferromagnetism of antiferromagnetics, *J. Phys. Chem. Solids* **4**, 241 (1958).
- [23] T. Moriya, Anisotropic superexchange interaction and weak ferromagnetism, *Phys. Rev.* **120**, 91 (1960).
- [24] A. Crépieux and C. Lacroix, Dzyaloshinsky-Moriya interactions induced by symmetry breaking at a surface, *J. Magn. Magn. Mater.* **182**, 341 (1998).
- [25] S. Rohart, A. Thiaville, Skyrmion confinement in ultrathin film nanostructures in the presence of Dzyaloshinskii-Moriya interaction, *Phys. Rev. B* **88**, 184422 (2013).
- [26] N. Nagaosa, Y. Tokura, Topological properties and dynamics of magnetic skyrmions, *Nat. Nanotechnol.* **8**, 899 (2013).
- [27] S. Mühlbauer, B. Binz, F. Jonietz, C. Pfleiderer, A. Rosch, A. Neubauer, R. Georgii, P. Böni, Skyrmion lattice in a chiral magnet, *Science* **323**, 915 (2009).
- [28] W. Münzer, A. Neubauer, T. Adams, S. Mühlbauer, C. Franz, F. Jonietz, R. Georgii, P. Böni, B. Pedersen, M. Schmidt, Skyrmion lattice in the doped semiconductor $\text{Fe}_{1-x}\text{Co}_x\text{Si}$, *Phys. Rev. B* **81**, 041203 (2010).
- [29] X.Z. Yu, Y. Onose, N. Kanazawa, J.H. Park, J.H. Han, Y. Matsui, N. Nagaosa, Y. Tokura, Real-space observation of a two-dimensional skyrmion crystal, *Nature* **465**, 901 (2010).

- [30] P. Milde, D. Köhler, J. Seidel, L. Eng, A. Bauer, A. Chacon, J. Kindervater, S. Mühlbauer, C. Pfleiderer, S. Buhrandt, Unwinding of a skyrmion lattice by magnetic monopoles, *Science* **340**, 1076 (2013).
- [31] X. Yu, N. Kanazawa, Y. Onose, K. Kimoto, W. Zhang, S. Ishiwata, Y. Matsui, Y. Tokura, Near room-temperature formation of a skyrmion crystal in thin-films of the helimagnet FeGe, *Nat. Mater.* **10**, 106 (2011).
- [32] S.X. Huang, C.L. Chien, Extended Skyrmion phase in epitaxial FeGe(111) thin films, *Phys. Rev. Lett.* **108**, 267201 (2012).
- [33] S. Heinze, K. Von Bergmann, M. Menzel, J. Brede, A. Kubetzka, R. Wiesendanger, G. Bihlmayer, S. Blügel, Spontaneous atomic-scale magnetic skyrmion lattice in two dimensions, *Nat. Phys.* **7**, 713 (2011).
- [34] W. Jiang, P. Upadhyaya, W. Zhang, G. Yu, M.B. Jungfleisch, F.Y. Fradin, J.E. Pearson, Y. Tserkovnyak, K.L. Wang, O. Heinonen, Blowing magnetic skyrmion bubbles, *Science* **349**, 283 (2015).
- [35] O. Boulle, J. Vogel, H. Yang, S. Pizzini, D. de Souza Chaves, A. Locatelli, T.O. Menteş, A. Sala, L.D. Buda-Prejbeanu, O. Klein, Room-temperature chiral magnetic skyrmions in ultrathin magnetic nanostructures, *Nat. Nanotechnol.* **11**, 449 (2016).
- [36] A.K. Nayak, V. Kumar, T. Ma, P. Werner, E. Pippel, R. Sahoo, F. Damay, U.K. Rossler, C. Felser, S.S.P. Parkin, Magnetic antiskyrmions above room temperature in tetragonal Heusler materials, *Nature* **548**, 561 (2017).
- [37] M. Hoffmann, B. Zimmermann, G.P. Muller, D. Schurhoff, N.S. Kiselev, C. Melcher, S. Blugel, Antiskyrmions stabilized at interfaces by anisotropic Dzyaloshinskii-Moriya interactions, *Nat. Commun.* **8**, 308 (2017).
- [38] S. Huang, C. Zhou, G. Chen, H. Shen, A.K. Schmid, K. Liu, Y. Wu, Stabilization and current-induced motion of antiskyrmion in the presence of anisotropic Dzyaloshinskii-Moriya interaction, *Phys. Rev. B* **96**, 144412 (2017).
- [39] S.L. Zhang, G. van der Laan, W.W. Wang, A.A. Haghighirad, T. Hesjedal, Direct Observation of Twisted Surface skyrmions in Bulk Crystals, *Phys. Rev. Lett.* **120**, 227202 (2018).
- [40] S. Zhang, G. van der Laan, J. Muller, L. Heinen, M. Garst, A. Bauer, H. Berger, C. Pfleiderer, T. Hesjedal, Reciprocal space tomography of 3D skyrmion lattice order in a chiral magnet, *PNAS* **115**, 6386 (2018).
- [41] A. Thiele, Steady-state motion of magnetic domains, *Phys. Rev. Lett.* **30**, 230 (1973).
- [42] M. J. Donahue and D. G. Porter, *OOMMF User's Guide, v. 1.0* (National Institute of Standards and Technology, Gaithersburg, MD, 1999); NIST Interagency Report No. NISTIR6376, 1999.
- [43] S.L. Zhang, G. van der Laan, T. Hesjedal, Direct experimental determination of the topological winding number of skyrmions in Cu₂OSeO₃, *Nat. Commun.* **8**, 14619 (2017).
- [44] X. Yu, K. Shibata, W. Koshibae, Y. Tokunaga, Y. Kaneko, T. Nagai, K. Kimoto, Y. Taguchi, N. Nagaosa, Y. Tokura, Thermally activated helicity reversals of skyrmions, *Phys. Rev. B* **93**, 134417 (2016).
- [45] Y. Yamane, J. Sinova, Skyrmion-number dependence of spin-transfer torque on magnetic bubbles, *J. Appl. Phys.* **120**, 233901 (2016).
- [46] K. Everschor, M. Garst, R. Duine, A. Rosch, Current-induced rotational torques in the skyrmion lattice phase of chiral magnets, *Phys. Rev. B* **84**, 064401 (2011).
- [47] K. Everschor, M. Garst, B. Binz, F. Jonietz, S. Mühlbauer, C. Pfleiderer, A. Rosch, Rotating skyrmion lattices by spin torques and field or temperature gradients, *Phys. Rev. B*, **86**, 054432 (2012).
- [48] J. Iwasaki, M. Mochizuki, N. Nagaosa, Universal current-velocity relation of skyrmion motion in chiral magnets, *Nat. Commun.* **4**, 1463 (2013).
- [49] N. Papanicolaou, T. Tomaras, Dynamics of magnetic vortices, *Nucl. Phys. B* **360**, 425 (1991).
- [50] C. Moutafis, S. Komineas, J. Bland, Dynamics and switching processes for magnetic bubbles in nanoelements, *Phys. Rev. B* **79**, 224429 (2009).
- [51] M. Knoester, J. Sinova, R. Duine, Phenomenology of current-skyrmion interactions in thin films with perpendicular magnetic anisotropy, *Phys. Rev. B* **89**, 064425 (2014).

Figures

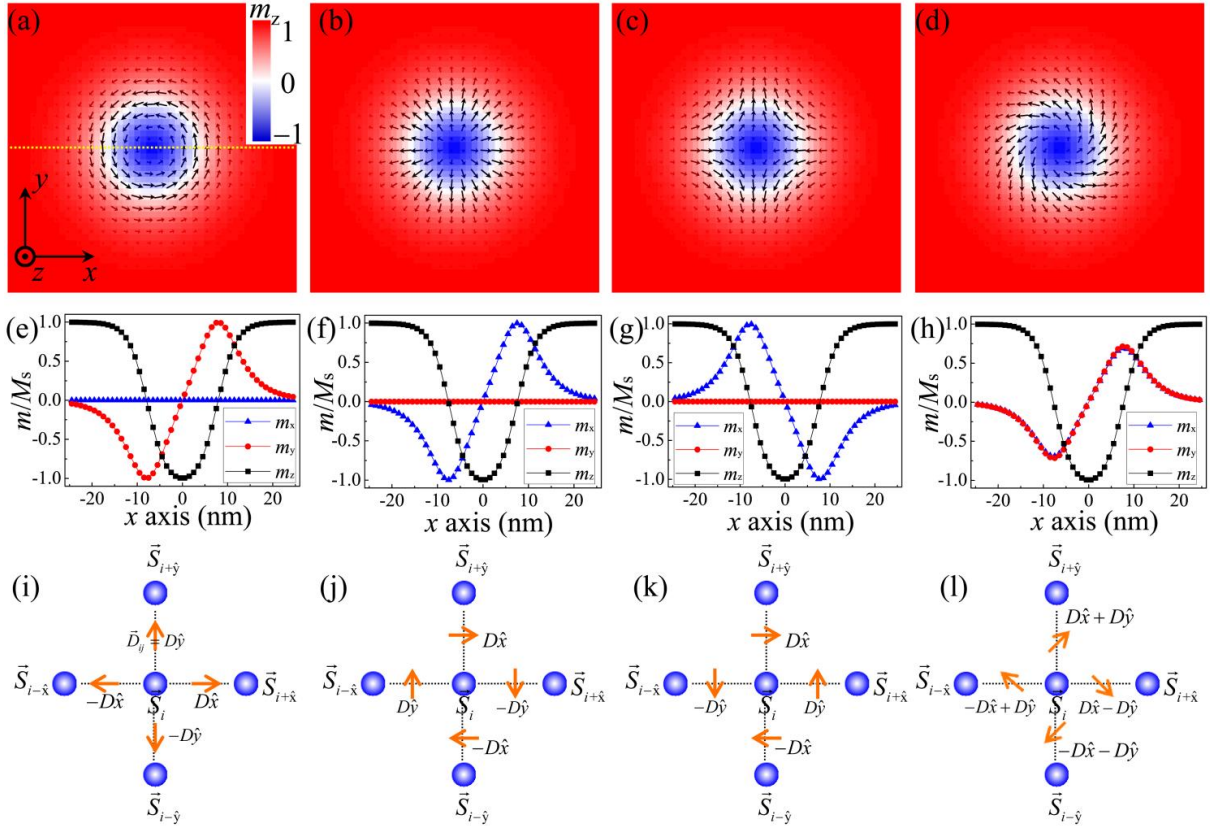


FIG. 1. Four types of skyrmions. (a)–(d) display the magnetization distribution of Bloch skyrmion, Néel skyrmion, antiskyrmion and twisted skyrmion, respectively. We only intercept the central region of the 2D plane with the size of $50 \text{ nm} \times 50 \text{ nm}$. The red, white and blue represent where the z component of the magnetization is positive, zero and negative, respectively. The black arrows denote the distribution of the in-plane magnetization. (e)–(h) are the spatial profiles of the local magnetization corresponding to the yellow dotted line which marked in the Fig. 1(a). (i)–(l) are the configurations of bulk DMI, interfacial DMI, anisotropic DMI and twisted DMI, respectively. The orange arrows denote the directions of the DMI vector.

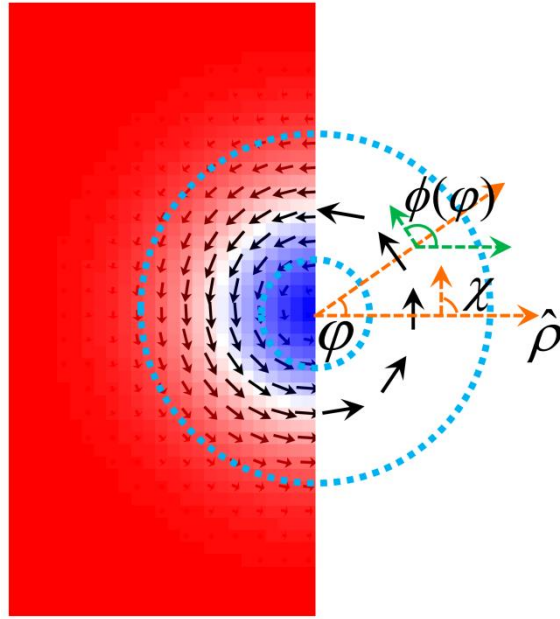


FIG. 2. Schematic of a general skyrmion in two-dimensional polar coordinates. ρ , φ , χ and $\phi(\varphi)$ indicate the radial coordinate, azimuthal angle, skyrmion helicity and the angle between the magnetic moment and the radial coordinate, respectively.

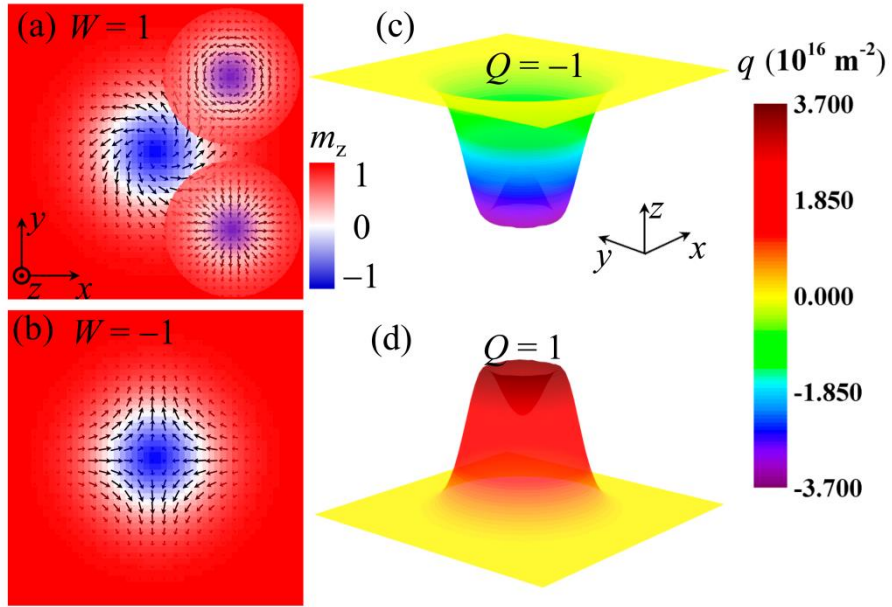


FIG. 3. (a) displays the magnetization distributions of twisted skyrmion, Bloch skyrmion and Néel skyrmion with $W = 1$. (b) displays the magnetization distribution of antiskyrmion with $W = -1$. (c) and (d) show the distributions of topological density corresponding to the magnetizations shown in (a) and (b) with $Q = -1$ and $Q = 1$, respectively.

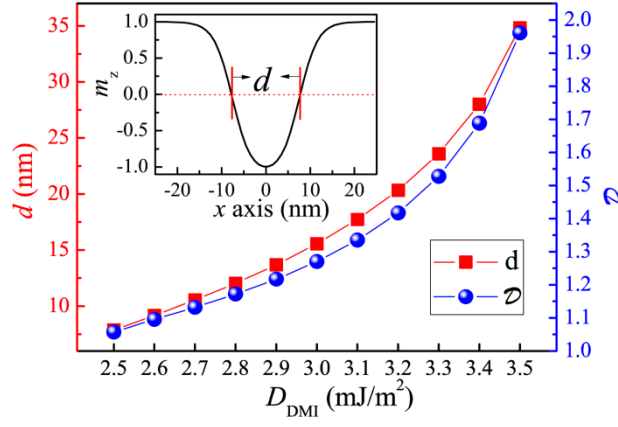


FIG. 4. Skyrmion diameter (d) and the diagonal element of the dissipative tensor (\mathcal{D}) as a function of DMI strength. The inset is the spatial profile of m_z across the twisted skyrmion. It should be note that the twisted skyrmion exists stably in region of $250 \text{ nm} \times 250 \text{ nm}$, the diagram only show the central part of $50 \text{ nm} \times 50 \text{ nm}$.

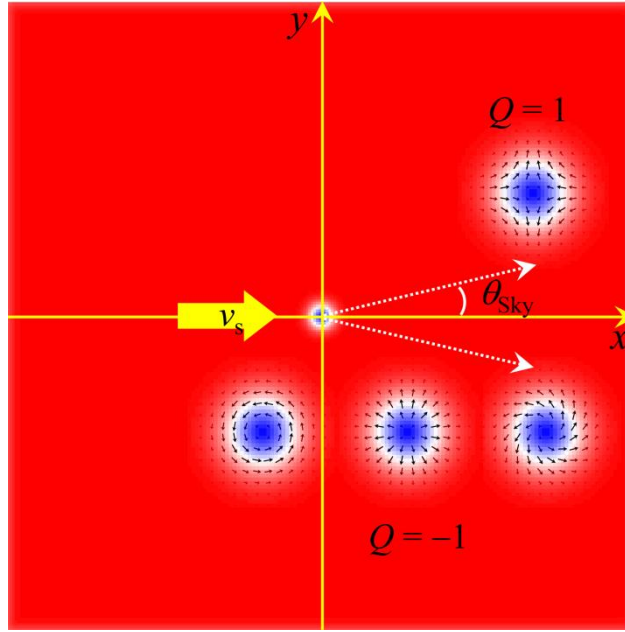


FIG. 5. The trajectories of four types of skyrmion driven by the STT. The initial position of the skyrmions is at the center of the 2D magnetic film, the size of 2D plane is $250 \text{ nm} \times 250 \text{ nm}$, $v_s = 100 \text{ m/s}$ in x direction, $\alpha = 0.4$, $\beta = 0.2$ and $D_{\text{DMI}} = 3 \text{ mJ/m}^2$. The big yellow solid arrow and white dotted arrows represent the direction of conduction electrons and the trajectories of skyrmions, respectively. It should be note that the four types of skyrmions are enlarged with the purpose to see their helicities clearly. The actual sizes of the four skyrmions are almost the same as the skyrmion at the center position.

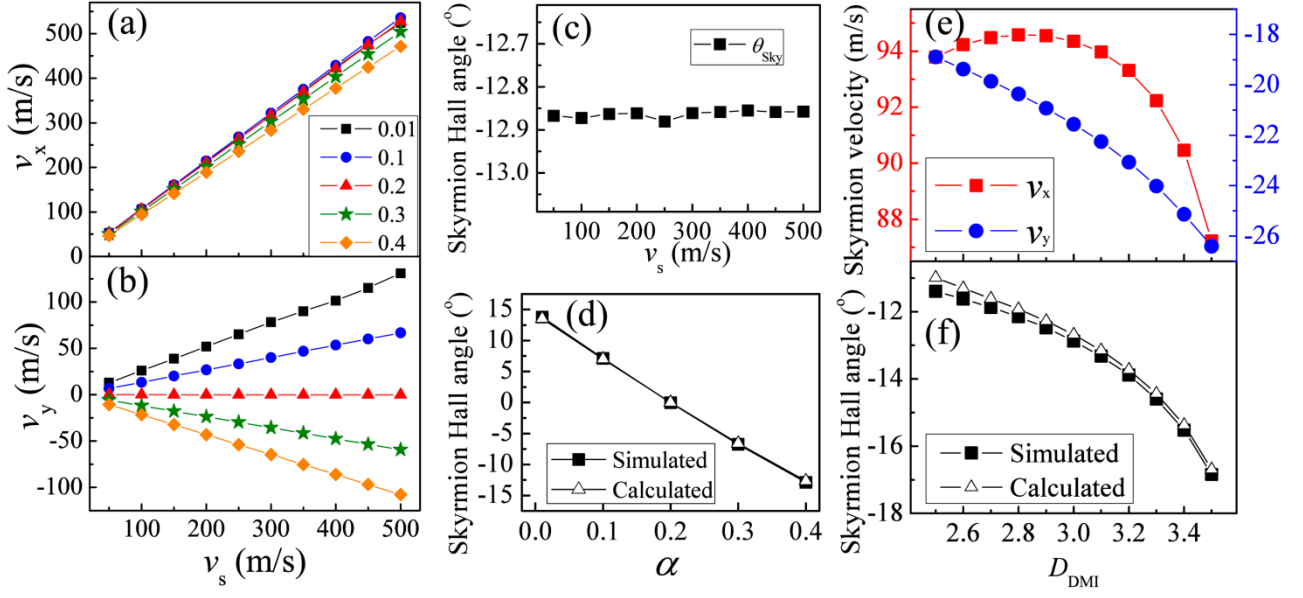


FIG. 6. The STT-induced motion of the twisted skyrmion ($\chi = 0.25\pi$). (a) and (b) display the v_x and v_y as a function of v_s for $\alpha = 0.01, 0.1, 0.2, 0.3$ and 0.4 with $\beta = 0.2$ and $D_{\text{DMI}} = 3 \text{ mJ/m}^2$, respectively. (c) The skyrmion Hall angle θ_{sky} as a function of v_s corresponding to the situation of $\alpha = 0.4$ shown in Figs. (a) and (b). (d) The skyrmion Hall angle θ_{sky} as a function of α corresponding to the situation of $v_s = 100 \text{ m/s}$ shown in Figs. 6 (a) and (b). (e) and (f) display the skyrmion velocity and the skyrmion Hall angle as a function of D_{DMI} with $v_s = 100 \text{ m/s}$, $\alpha = 0.4$ and $\beta = 0.2$, respectively.

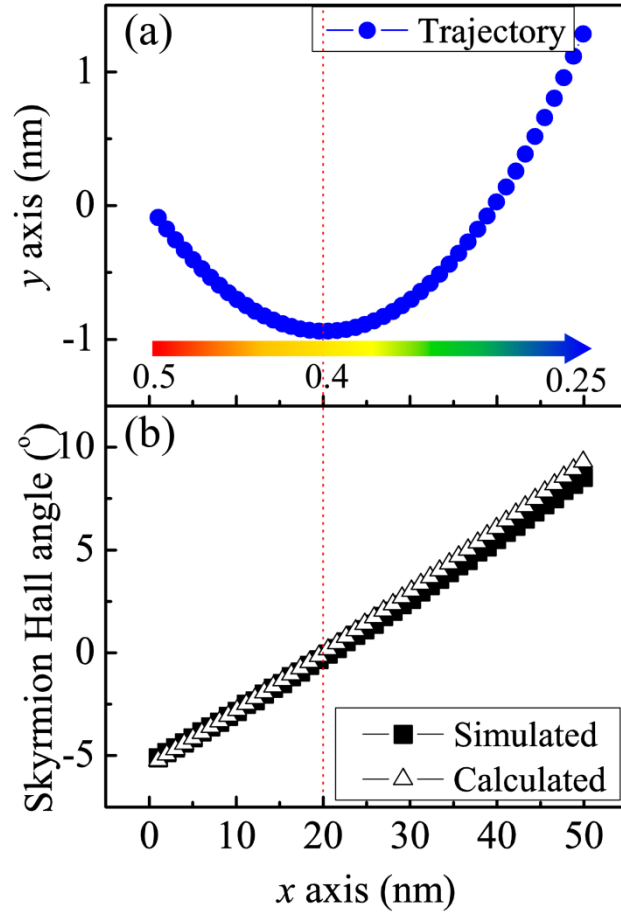


FIG. 7. The STT-induced motion of the twisted skyrmion under a damping gradient. (a) and (b) show the transverse distance (y axis) of the skyrmion and the corresponding skyrmion Hall angle θ_{sky} as a function of radial distance (x axis), respectively. The initial position of the skyrmions is defined as 0 nm both in x and y axis, $v_s = 100$ m/s, $\beta = 0.4$ and $D_{\text{DMI}} = 3$ mJ/m². The color code represents that the damping α decreases from 0.5 to 0.25 linearly in the region from 0 to 50 nm along the x direction. The red dotted line represents the position where $\alpha = \beta$.

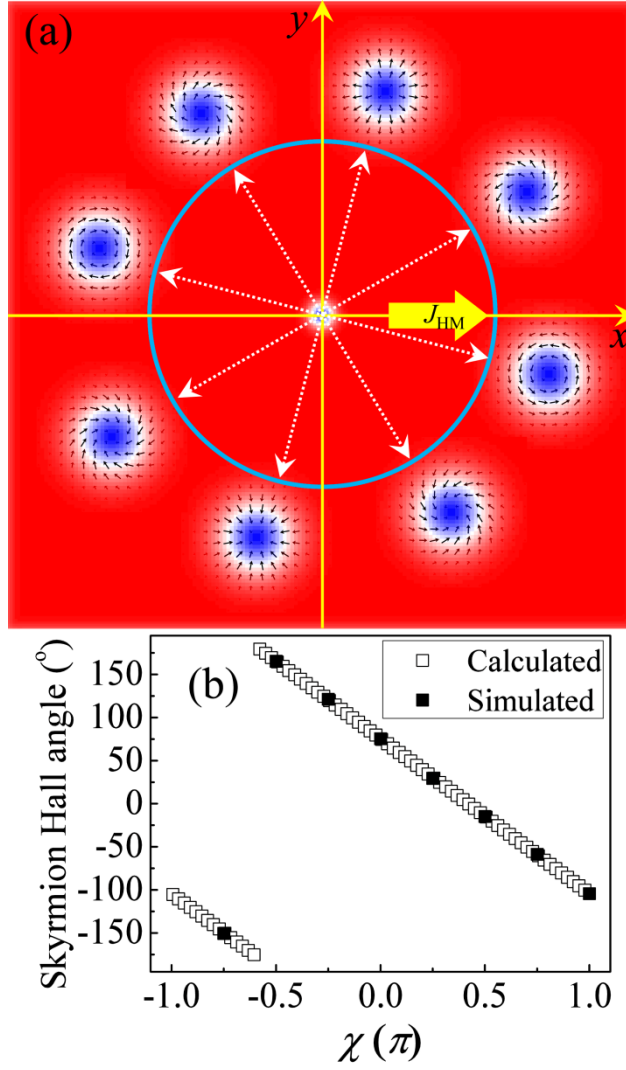


FIG. 8. The SHE-induced motion of skyrmions with different χ (a) The trajectories of eight types of skyrmions with $\chi = -0.75\pi, -0.5\pi, -0.25\pi, 0, 0.25\pi, 0.5\pi, 0.75\pi$ and π driven by the SHE. The initial position of the eight skyrmions is in the center of the 2D magnetic film whose size is $250 \text{ nm} \times 250 \text{ nm}$, $\alpha = 0.2$ and $D_{DMI} = 3 \text{ mJ/m}^2$. The big yellow solid arrow denotes the direction of current $J_{HM} = 10 \times 10^{10} \text{ A/m}^2$. The white dotted arrows represent the trajectories of skyrmions. It also should be note here that the eight types of skyrmions are enlarged to see their helicities clearly. The actual sizes of the eight skyrmions are almost the same as them at the center position. (b) The skyrmion Hall angle θ_{sky} as a function of the helicity χ . The black solid squares correspond to the eight types of skyrmion in Fig. 8(a), and the black hollow squares are calculated by the equation.

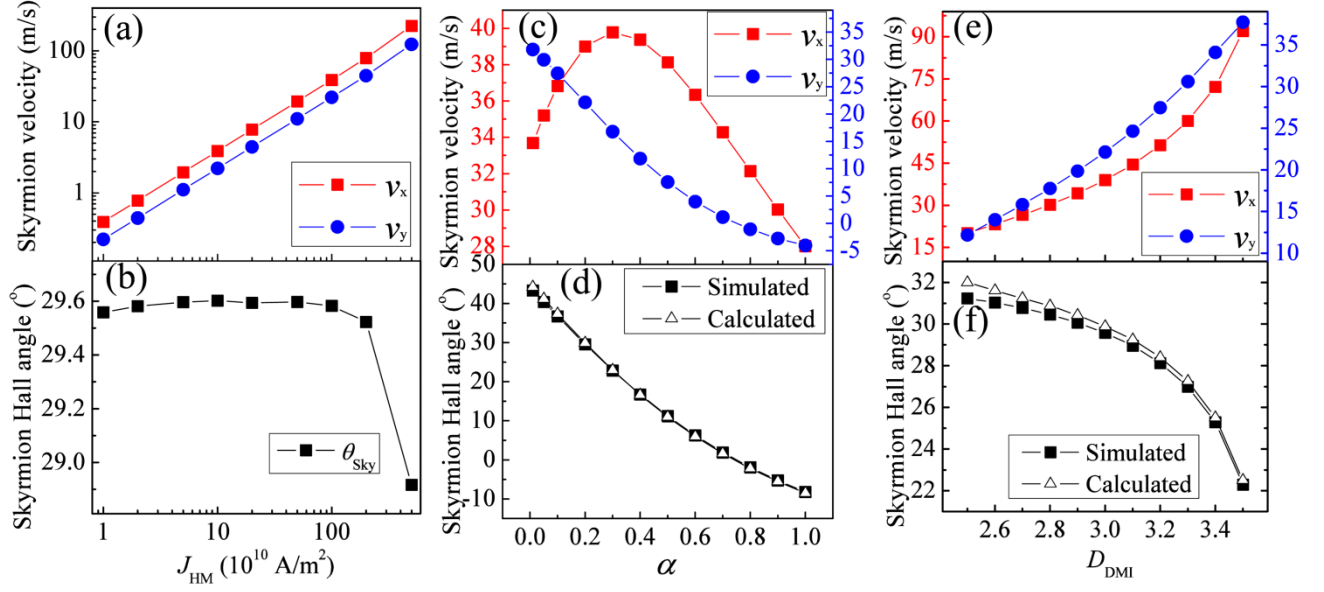


FIG. 9. The SHE-induced motion of the twisted skyrmion ($\chi = 0.25\pi$). (a) and (b) display the skyrmion velocity and skyrmion Hall angle θ_{sky} as a function of J_{HM} with $\alpha = 0.2$ and $D_{\text{DMI}} = 3$ mJ/m², respectively. (c) and (d) denote the skyrmion velocity and skyrmion Hall angle θ_{sky} as a function of α with $J_{\text{HM}} = 100 \times 10^{10}$ A/m² and $D_{\text{DMI}} = 3$ mJ/m², respectively. (e) and (f) represent the skyrmion velocity and skyrmion Hall angle θ_{sky} as a function of D_{DMI} with $J_{\text{HM}} = 100 \times 10^{10}$ A/m² and $\alpha = 0.2$, respectively.

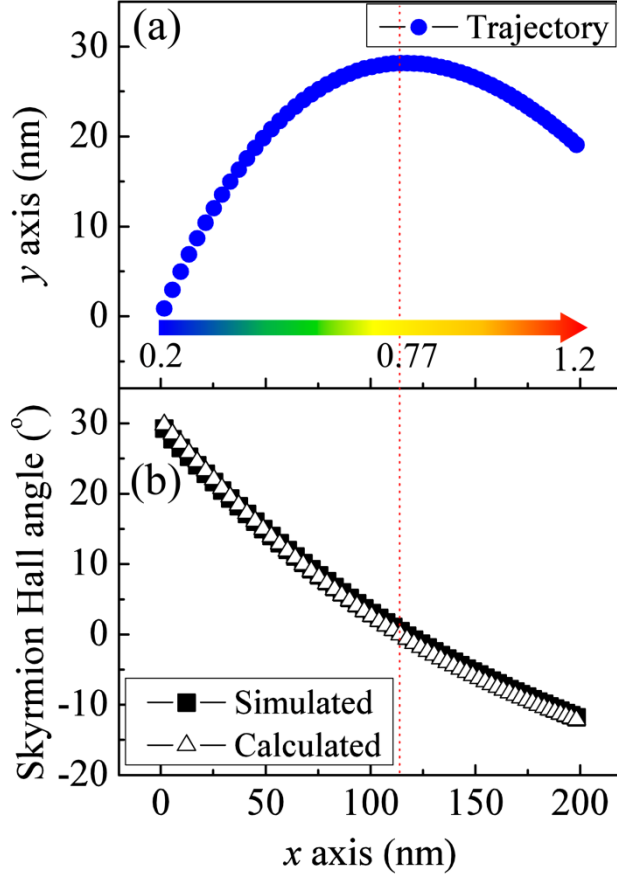


FIG. 10. The SHE-induced motion of the twisted skyrmion under a damping gradient. (a) and (b) show the transverse distance (y axis) of the skyrmion and the corresponding skyrmion Hall angle θ_{sky} as a function of radial distance (x axis), respectively. The initial position of the skyrmions is defined as 0 nm both in x and y axis, $J_{\text{HM}} = 100 \times 10^{10} \text{ A/m}^2$ and $D_{\text{DMI}} = 3 \text{ mJ/m}^2$. The color code represents that the damping α increases from 0.2 to 1.2 linearly in the region from 0 to 200 nm along the x direction. The red dotted line represents the position where $1 - \alpha \mathcal{D} = 0$, i.e., the skyrmion Hall angle $\theta_{\text{sky}} = 0^\circ$.